lajss.org©
Latin American Journal of Solids and Structures
www.lajss.org

Formation and Penetration Damage Effects of Uniform-Thickness Liner TEFPs on Metal Targets

Qingxin QIN[a*] 0009-0009-6343-490X, Chong Ji[a] 0000-0003-3428-6302, Xin Wang[a*] 0000-0002-9572-9288, Yuxuan Gao[a] 0009-0008-8616-3236,Gang Wu [a]0000-0003-3043-3336, Weijian Tang [a] 0009-0005-8351-6196

[a] College of Field Engineering, Army Engineering University of PLA, Nanjing 210007, China. E-mails:

3449608540@qq.com; 2468645816@qq.com; 310433804@qq.com; 2099108489@qq.com;wugangimpact@aeu.edu.cn;2454566100@qq.com

* Corresponding author

Abstract

This study investigates a toroidal explosively formed projectile (TEFP) warhead with an 88 mm charge diameter and uniform-thickness liners. Normal penetration experiments on double-layer Q235 steel targets were conducted at varying stand-off distances and liner thicknesses (3 mm and 4.5 mm), complemented by LS-DYNA simulations to analyze TEFP formation and penetration behavior. Increasing stand-off distance and liner thickness enlarge the penetration hole diameter but reduce penetration capability and behind-armor damage, with the hole-bottom failure mode transitioning from shear to tension. Grain evolution at hole sidewalls proceeds through dynamic recrystallization, severe elongation, and distorted deformation. Based on the impact angle θ, three penetration modes are identified: positive cutting (0° < θ ≤ 85°), accurate cutting (85° < θ ≤ 95°), and reverse cutting (95° < θ < 180°).

Keywords
TEFP, liner thickness, stand-off distance, numerical simulation, penetration mode

1 INTRODUCTION

Rapid urbanization and industrial expansion have intensified the demand for efficient emergency breaching in extreme environments (e.g., post-disaster rescue, shipwreck salvage). Traditional mechanical and laser methods often suffer from low efficiency, cumbersome equipment, and spatial constraints. In contrast, detonation-driven shaped charges offer superior energy density and instantaneous response.

In shaped charge breaching, the morphology of the penetrator directly determines the quality and efficiency of hole opening. Researchers have extensively studied three typical penetrator classes: shaped charge jets (SCJ), explosively formed projectiles (EFP), and jetting projectile charges (JPC). A comprehensive overview of the advances in shaped charge technology over the past two decades was provided by Mehmannavaz et al. (2021), who systematically reviewed progress in liner materials, explosive formulations, and numerical simulation techniques that have collectively elevated modern shaped charge performance. At the material level, introducing low-impedance or reactive materials effectively enhances lateral hole-expansion. At the structural level, Shen et al. (2025) recently classified the novel liner configurations developed in recent years—including shaped, segmented, and composite liners—and highlighted their respective influences on jet/EFP formation stability and penetration capability, providing a useful framework for understanding the structural design space of advanced shaped charge warheads. Wang et al. (2018) showed that aluminum liners produce larger hole diameters in targets than copper liners, which are typically optimized for penetration depth. Guo et al. (2019) incorporated reactive materials into liners (RLSCJ) and found that reactive jets sacrifice some penetration depth in thick steel plates to achieve significantly larger perforation diameters. In particular, within a stand-off distance (SD) of 0.5 to 1.5 charge diameters (CD), RLSCJs induce strong behind-armor debris effects, substantially improving the overall hole-expansion performance. Extending this concept, Zhang et al. (2022) investigated reactive liner shaped charges specifically for concrete targets and reported that the sequential action of kinetic penetration followed by chemical energy release from reactive fragments substantially enlarges the damaged zone—an effect of direct relevance to breaching applications where maximizing perforation diameter is the primary objective.

For EFPs, the trade-off between penetration depth and hole diameter is also dominated by material characteristics. Liu et al. (2017) verified that pure copper EFPs achieve a maximum penetration depth twice that of iron EFPs. Beyond material substitution, the charge configuration itself can be leveraged to tailor EFP output. Liu et al. (2020) demonstrated that double-layer explosive charges—pairing a high-detonation-velocity explosive with a lower-velocity one—generate an axial gradient of detonation energy release, which enhances EFP velocity and compactness without modifying the liner geometry. This suggests that charge-structure optimization can serve as a complementary strategy to liner thickness variation for regulating penetrator characteristics. Conversely, Han et al. (2019) designed zirconium/tantalum double-layer composite liners and discovered that reducing the thickness ratio of the inner and outer liners enhances hole-expansion and radial tearing, although tip velocity and penetration depth decrease. At the level of charge configuration and structural parameters, researchers can also improve hole-opening efficiency by regulating mass distribution and the stretching state of the penetrator. Cardoso and Teixeira-Dias (2016) confirmed through numerical prediction that liner thickness variation decisively influences EFP formation and terminal ballistic performance. Chen et al. (2015) designed an eccentric sub-hemispherical variable-thickness liner with a "thick-top and thin-edge" configuration, successfully increasing the effective jet mass by 29.5%. This optimization of mass and momentum distribution provides a physical basis for enlarging the hole-opening area. Dehestani et al. (2018) noted that a moderate increase in stand-off distance facilitates jet stretching, but exceeding a critical value leads to penetrator fragmentation and velocity attenuation, severely weakening penetration and hole-expansion. To maintain effective hole-opening at large stand-off distances, Fu et al. (2013) performed configuration optimization for JPCs and found that spherical liners achieve optimal comprehensive penetration performance at large standoffs, though the maximum penetration diameter is limited to 0.5 CD.

Despite these advances, traditional shaped charge technology inherently limits the perforation diameter to only 0.3–0.7 CD. This efficiency has reached a bottleneck for engineering rescue scenarios that require large-diameter breaching. To overcome the limitations of single-mode warheads, Yin et al. (2023) proposed a multimode concept capable of switching between PELE (Penetrator with Enhanced Lateral Effect) and EFP modes within a single charge, demonstrating that the integration of multiple damage mechanisms can address the diverse operational requirements encountered in complex breaching scenarios. Consequently, researchers have initiated investigations into innovative charge structures with enhanced radial hole-expansion capabilities. Li et al. (2025a, 2025b) conducted in-depth studies on asymmetric annular and asymmetric hollow structures. They indicated that, driven by asymmetric detonation waves, these configurations effectively alter the radial velocity gradient of the jet head, producing a more pronounced lateral hole-expansion effect on metal targets compared to conventional jets. Xu et al. (2019) investigated bore-center annular shaped charges and confirmed that the central bore design can transfer more energy from the liner toward the periphery of the target area. When combined with different metals, these charges exhibit excellent plugging and large-area perforation capabilities. Yang et al. (2022) introduced a closed-cell W-shaped liner. By optimizing the W-shaped bottom angle and geometric parameters, they achieved a uniform radial distribution of charge energy, significantly enhancing terminal hole-expansion performance. Ji et al. (2021) fabricated liners from lightweight non-metallic materials (e.g., nylon) and found that low-density, high-velocity nylon jets, upon high-speed impact, induce extremely strong radial scouring damage, thereby enlarging penetration hole diameter.

The Toroidal Explosively Formed Projectile (TEFP), which can achieve ultra-large perforation diameters of up to 1.6 times the charge caliber through global plugging and shearing to enhance breaching efficiency, is an excellent candidate for large-diameter breaching applications due to its large radial dimension and plugging-mode penetration. Richard et al. (2010) proposed a new paradigm for shaped-charge breaching: the Toroidal Explosively Formed Projectile (TEFP). They successfully achieved regular circular holes with diameters as large as 2.1 CD, convincingly validating the feasibility and technical superiority of TEFPs for ultra-large-diameter breaching tasks. Hu et al. (2026) systematically analyzed the formation mechanisms and penetration performance of TEFPs. Their research demonstrated that the TEFP abandons the fragmentation-prone jet-stretching mechanism. Instead, it relies on controlled inversion of the liner driven by detonation waves to consolidate into a high-density toroidal penetrator with exceptional structural integrity. This configuration triggers a powerful full-section plugging and shearing effect upon impact. Furthermore, Tang et al. (2025) investigated the influence of stand-off distance on TEFP penetration characteristics. They noted that the morphological evolution and kinetic energy distribution of the TEFP during flight vary significantly with stand-off distance, directly governing the dynamic trade-off between penetration depth and hole-expansion diameter.

However, the existing literature on TEFPs has focused primarily on formation mechanisms and general feasibility. The influence of key design parameters, especially liner thickness, on TEFP penetration performance remains inadequately understood. Moreover, although Tang et al. (2025) examined stand-off distance effects, their study did not systematically couple stand-off distance with liner thickness for uniform-thickness configurations. This gap is critical because uniform-thickness liners—offering simplicity and reproducibility—are promising for practical engineering applications, yet no parametric study has quantified how liner thickness and stand-off distance jointly affect the penetration performance of TEFPs.

In this work, the penetration of Q235 steel targets using an 88-mm diameter TEFP with a uniform-thickness liner is experimentally investigated. The experiments are complemented with validated numerical simulations of both the formation and penetration processes. The objective is the characterization of the TEFP evolution and damage mechanisms, specifically the elucidation of the correlation between liner thickness, stand-off distance, and penetration effectiveness. A parametric basis for designing TEFP charges with predictable hole-opening performance is provided by the findings.

2 CONFIGURATIONS OF THE EXPERIMENTAL APPARATUS

The warhead structure of the uniform-thickness liner TEFP primarily comprises a metal liner, charge, a casing, and a detonator. The geometric configuration of the uniform-thickness liner is defined by four key dimensional parameters: the wall thickness a (a = b), the liner diameter d, the inner arc radius R_1, and the outer arc radius R_2. The charge is composed of an RDX-based mixed explosive, characterized by a density of 1.304 g/cm^3.a charge diameter (CD) of 88 mm, and a charge height of 52.8 mm. The casing, fabricated from resin material via 3D printing, functions to secure the explosive charge. To investigate the penetration effects and the impact of wall thickness of the TEFP, two uniform-thickness liners were designed with thicknesses of 3 mm and 4.5 mm, respectively. Both liners feature a diameter of 88 mm and internal and external radii of curvature of 130 mm. The wall thickness and stand-off distance are adopted as the primary variables in this study, and their effects on TEFP formation and penetration performance constitute the main research objective of this paper.

Figure 1 illustrates the schematic diagram of the experimental setup for the target penetration by the uniform-thickness liner TEFP warhead. The setup primarily comprises four components: a detonator, the TEFP warhead, a standoff tube, and a target stand. The standoff tube is fabricated from kraft paper, and the influence of its mechanical strength on the formation and penetration processes is negligible. Supported by the standoff tube, the warhead is vertically secured above the target, and the stand-off distance is controlled by adjusting the length of the tube. Q235 steel was selected as the target material for the following reasons. First, as a widely used low-carbon structural steel in civil and marine engineering, Q235 represents the typical material encountered in emergency breaching scenarios such as post-disaster rescue and shipwreck salvage, making it directly relevant to the practical application context of this study. Second, Q235 possesses well-characterized and stable mechanical properties, providing a standardized baseline for evaluating TEFP penetration performance and enabling meaningful comparisons with existing shaped-charge penetration data in the literature. Third, the relatively low strength and high ductility of Q235 allow clear differentiation of penetration hole morphologies—including the plastic hole-expansion zone, shear zone, and copper-plating phenomenon—under varying liner thicknesses and stand-off distances, which facilitates a systematic analysis of the underlying damage mechanisms. The targets are classified into a main target (A) and a witness target (B). Both targets possess dimensions of 500 mm × 500 mm × 10 mm and are separated by a spacing of 30 mm. They are securely fastened by a steel frame to restrict lateral displacement. To analyze the effects of stand-off distance and wall thickness on the formation and penetration performance of the TEFP, penetration experiments were conducted on the two liner structures with different wall thicknesses at stand-off distances of h = 160 mm and 200 mm, respectively.

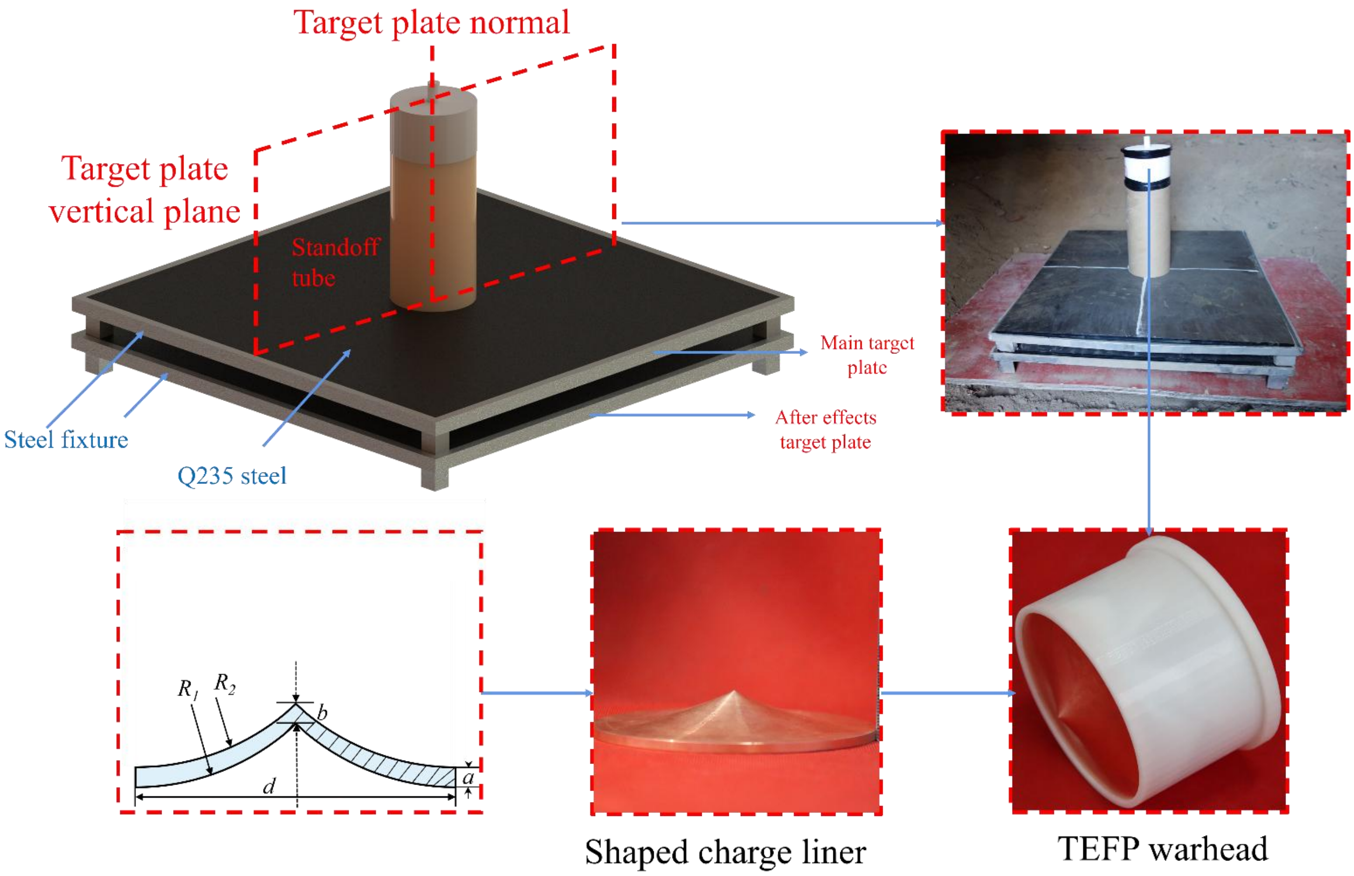

Figure 1 *Schematic diagram of the experimental apparatus for TEFP warhead penetration tests*

3 EXPERIMENTAL RESULTS AND ANALYSIS

3.1 Macroscopic Damage Morphology and Analysis

Figures 2 and 3 illustrate the macroscopic damage results of the uniform-thickness liner TEFPs with different wall thicknesses at h=160 mm and 200 mm. It is observed that at a stand-off distance of 160 mm, the TEFPs generated by both wall thicknesses can completely perforate the main target (Target A), resulting in continuous annular penetration holes. Both the perforation diameter and the diameter of the shear plugs increase progressively with the wall thickness. Notably, a significant fragment damage zone is observed surrounding the penetration hole on the front surface of Target A, with an area substantially exceeding the diameter of the hole itself. The analysis indicates that under the influence of detonation waves and detonation products, a portion of the TEFP material initially fragments. These fragments subsequently impact Target A, leading to the formation of the observable fragment damage zone. Cross-sectional observations of the perforated targets reveal a pervasive "copper-plating" phenomenon on the internal surfaces of the penetration holes. This occurs because the high-speed impact of the TEFP induces a localized extreme environment characterized by high temperature, high pressure, and high strain rates, which triggers intense plastic deformation of the copper liner material. Simultaneously, under these conditions, the oxygen-free copper exhibits enhanced adhesion, causing it to bond to the inner walls of the hole. Furthermore, the penetration region across the target thickness exhibits two distinct zones: the upper portion is a plastic hole-expansion zone characterized by a relatively smooth surface and a lip-like flange at the entrance formed by material eversion; the lower portion is a shear zone, displaying a typical rough fracture morphology.

At a stand-off distance of h=160 mm, the TEFPs generated by both uniform-thickness liners successfully perforate the main target (Target A) and continue to penetrate the witness target (Target B). This secondary penetration induces varying degrees of bending deformation in Target B and creates an annular distribution of copper pits on its front surface. A comparative analysis reveals that the 4.5 mm TEFP produces a larger damage zone diameter on Target B, yet its copper pits are markedly shallower than those produced by the 3 mm TEFP (average depth: 0.9 mm, compared with 2.1 mm for the 3 mm case), and the overall damage severity is correspondingly lower. This indicates that at this stand-off distance, although the thicker-walled TEFP possesses a superior hole-opening capability, its comprehensive penetration performance and residual damage effect are inferior to those of the thinner-walled structure. As the stand-off distance increases to h=200mm, the extent of the fragment damage zone on the front surface of Target A is significantly larger than the perforation diameter. This further corroborates that the TEFP undergoes localized fragmentation during the early stages of formation. Regarding the morphology of the penetration hole, the TEFP with a 3mm wall thickness still generates a continuous annular hole. In contrast, the perforation morphology produced by the 4.5mm thick TEFP transitions from the continuous annular shape observed at h=160 mm to a discontinuous configuration. This demonstrates that the residual TEFP gradually undergoes global fracture as the flight distance increases. Furthermore, a greater wall thickness correlates with higher sensitivity to variations in stand-off distance, leading to an earlier onset of fracture and a more pronounced degradation in penetration performance.

The damage manifestation on Target B also attenuates with the increase in stand-off distance. For the 3 mm TEFP, although it still perforates Target A and continues to impact Target B at h = 200 mm, forming annular copper pits, the average pit depth declines from 2.1 mm at h = 160 mm to 1.2 mm, and the overall damage severity drops markedly. The 4.5 mm TEFP exhibits an even sharper degradation: its average pit depth falls from 0.9 mm at h = 160 mm to zero at h = 200 mm, where it causes only bending deformation of Target B (maximum deflection: 3.2 mm) with no observable copper pits, indicating a complete loss of residual penetration capability on the witness target. Consequently, it is evident that the residual damage effectiveness of the TEFP gradually diminishes as the stand-off distance increases.

Synthesizing the macroscopic damage results of the two uniform-thickness liner TEFPs under various stand-off distances, the following conclusions can be drawn: The TEFP undergoes localized material fragmentation during the early stages of formation, yielding early-stage fragments and a damage zone; the remaining structure subsequently experiences global fracture after traveling a certain distance. Although the perforation diameter increases progressively with the stand-off distance and wall thickness, both the perforation capability and the residual damage effectiveness of the TEFP decrease accordingly. Furthermore, the thicker-walled TEFP exhibits a higher sensitivity to variations in stand-off distance, undergoing fracture within a shorter flight distance, which results in a marked degradation of its penetration performance.

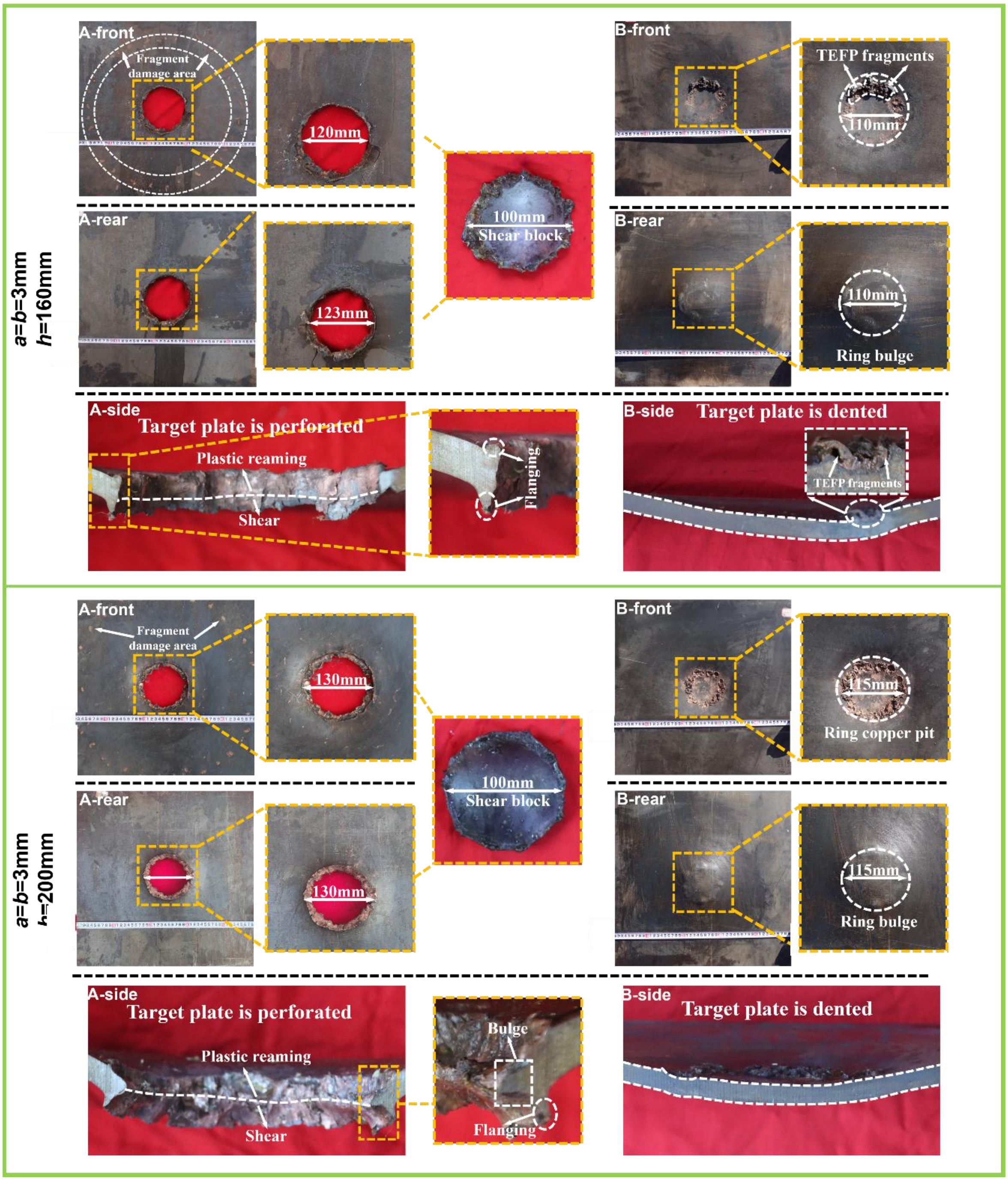

Figure 2 *Penetration damage results of the uniform-thickness liner TEFP warhead (a=3mm) at different stand-off distances*

Figure 3 *Penetration damage results of the uniform-thickness liner TEFP warhead (a=4.5mm) at different stand-off distances*

Figure 4 presents a comparison of the entrance and exit perforation diameters of Target A and the deformation dimensions of Target B at various stand-off distances. It is observed that although the perforation diameter generated by the uniform-thickness liner TEFP increases progressively with wall thickness and stand-off distance, its effective penetration and damage capability conversely diminish (specifically, the TEFP with a=4.5mm failed to perforate the target plate at h=200mm). Furthermore, the bending deformation and the overall degree of damage induced by the TEFP on the witness target exhibit a downward trend as both the wall thickness and stand-off distance increase.

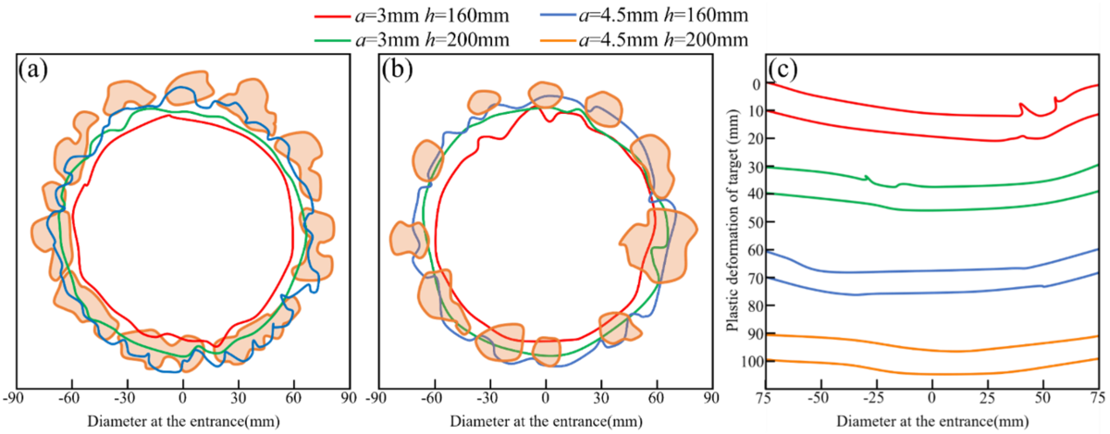

Figure 4 *Comparison of penetration hole dimensions of the uniform-thickness liner TEFP: (a) Entrance hole diameter of Target A; (b) Exit hole diameter of Target A; (c) Deformation of Target B*

3.2 Microscopic Damage Results and Analysis

3.2.1 Fracture Morphology Analysis of Metal Targets Penetrated by TEFPs from Uniform-Thickness Liners

Figures 5 and 6 illustrate the fracture morphologies of Q235 steel targets impacted by uniform-thickness liner TEFPs with wall thicknesses of a=3mm and a=4.5mm at stand-off distances of h=160mm and 200mm, respectively. A comparative analysis of these results systematically reveals the influence of wall thickness and stand-off distance on microscopic penetration damage. In the entrance region, the high-speed impact of both TEFP configurations induces intense plastic deformation and the formation of flanging, characterized by a dense distribution of fine dimples on the surface—a typical manifestation of a shear-stress-dominated deformation mode. This morphology originates from the localized extreme environment of high temperature, high pressure, and high strain rate generated upon impact. Under such conditions, micro-voids undergo rapid nucleation and coalescence within an extremely short duration, leading to the observed fine dimple size. Notably, for the thicker-walled structure (a=4.5mm), the dimple size at the entrance increases at h=200mm, accompanied by prominent micro-cracks. This phenomenon is attributed to the earlier fracture and diminished penetration capability of the TEFP caused by the increased wall thickness and stand-off distance. Consequently, the interaction time between the projectile and the target in the entrance region is prolonged, providing sufficient time for the micro-voids to grow and coalesce.

Along the penetration sidewall, as the velocity and strain rate of the TEFP decrease, the material is afforded sufficient time for plastic flow. Consequently, the dimple size on the sidewall is generally larger than that observed in the entrance region. However, as the stand-off distance increases, the microscopic damage (such as micro-cracks and voids) on the sidewalls induced by both TEFP configurations is mitigated. Specifically, for the TEFP with a=3mm at h=200mm, only fine micro-voids are observed on the sidewall, which reflects the attenuation of penetration kinetic energy with increasing stand-off distance.

The variation in failure modes within the bottom region is particularly pronounced. For the TEFP with a=3mm at h=160mm, the dimples in the bottom region are significantly elongated along the impact direction and subsequently ruptured, which is indicative of a localized shear failure. As the stand-off distance increases to h=200mm, although the dimples rupture to form voids, they lack significant elongation, demonstrating a transition in the failure mode towards localized tensile failure. Conversely, for the a=4.5mm TEFP, even at h=160mm, the dimples exhibit rupture without prior elongation, characterizing a localized tensile failure. When the stand-off distance is further elevated to h=200 mm, severe structural fracture and insufficient kinetic energy prevent the projectile from reaching the bottom. Consequently, this region is subjected solely to the propagation of stress waves, resulting in the formation of fine dimples without the appearance of voids.

In summary, with the increase in wall thickness and stand-off distance, the penetration capability of TEFP gradually decreases. This trend is manifested in the microscopic fracture morphology as follows: the prolonged interaction time in the entrance region may result in larger dimples and microcracks; the damage along the sidewalls is alleviated; and the failure mode at the bottom transforms from shear-dominated to tension-dominated. When the kinetic energy is insufficient, only micro void nucleation induced by stress waves occurs. These microscopic observations are consistent with the macroscopic finding that the penetration capability weakens as the wall thickness and stand-off distance increase, further elucidating the microscopic mechanism of TEFP damage behavior under the coupled influence of multiple parameters.

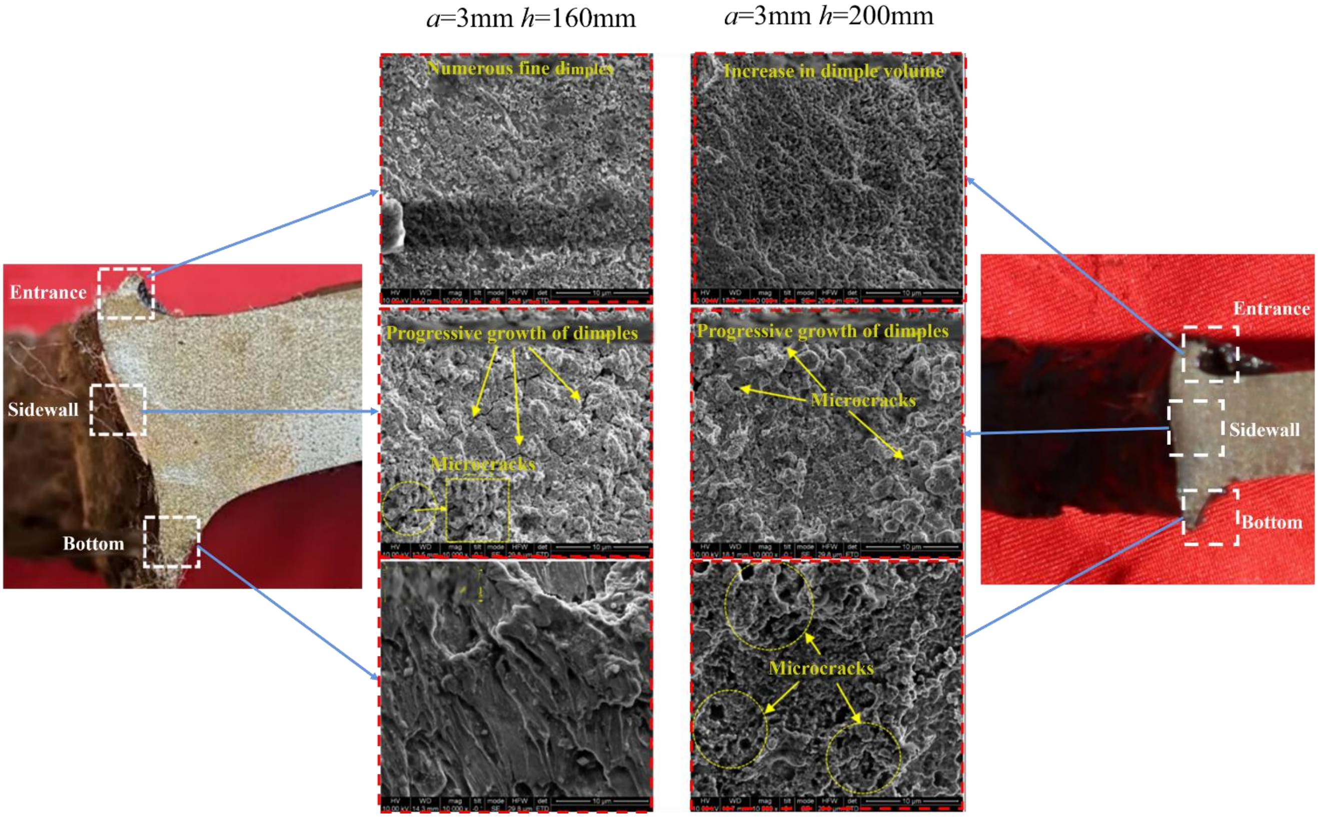

Figure 5 *Fracture morphology features of metal targets impacted by the uniform-thickness liner TEFP (a=3mm) at different stand-off distances*

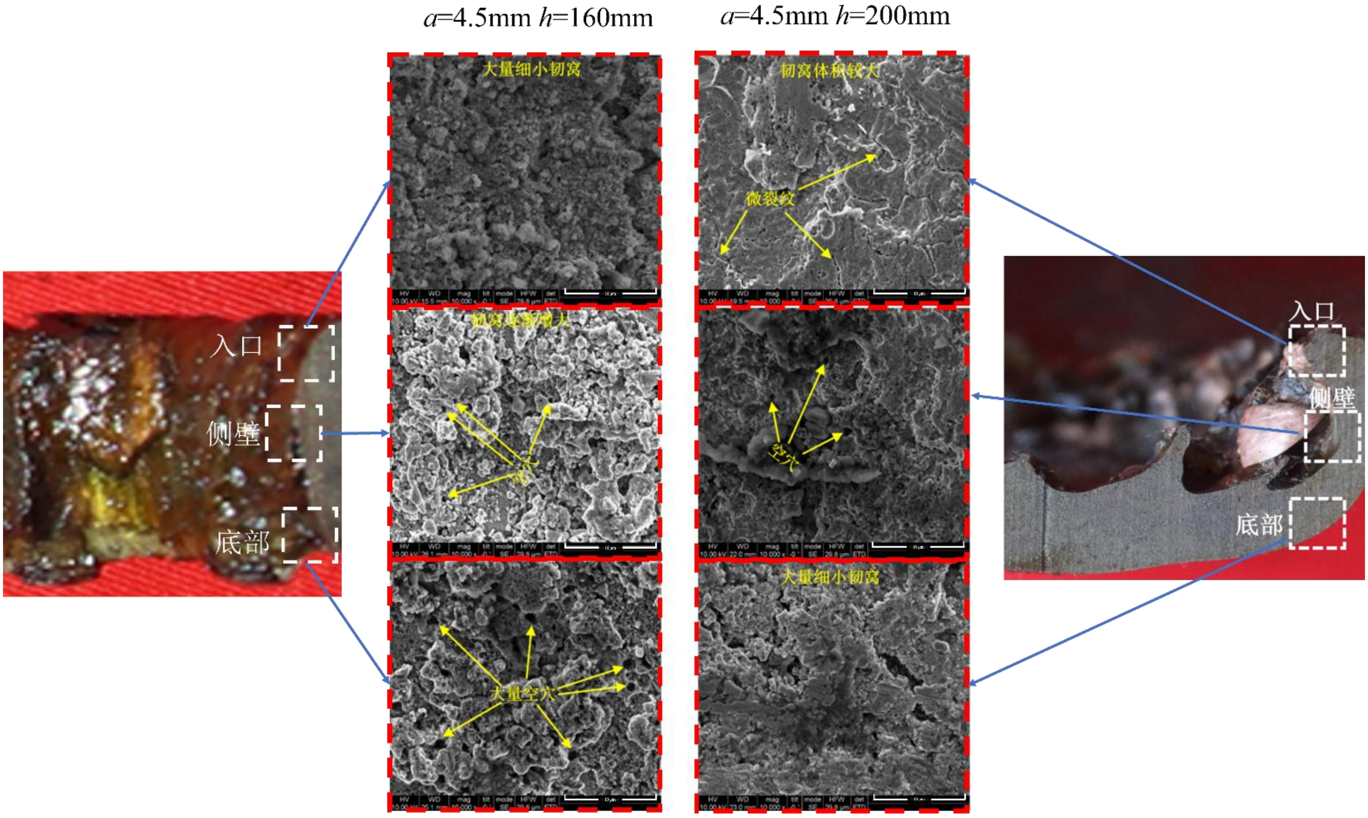

Figure6 *Fracture morphology features of metal targets under high-velocity impact of TEFPs (a=4.5mm uniform-thickness liner) at different stand-off distances*

3.2.2 Grain Evolution Analysis of Metal Targets Penetrated by TEFPs from Uniform-Thickness Liners

For the TEFP with uniform wall thickness impacting a steel target at various stand-off distances, the microstructural characteristics of the metallic grains along the sidewall are adjacent to the region of severe plastic deformation (SPD) in the target metal, as shown in Figure 7. It can be observed that a dynamic recrystallization zone forms near the sidewall of the penetration hole under all operating conditions. Outside this zone, the grains are significantly elongated due to intense plastic deformation (SPD); however, as the material has not yet undergone fragmentation, reorganization, and regrowth, dynamic recrystallization does not occur in this region.

It is noteworthy that, at the same stand-off distance, the width of the dynamic recrystallization zone decreases gradually with increasing wall thickness. Since high strain and high strain rate are essential conditions for initiating dynamic recrystallization, this phenomenon directly indicates that the strain and strain rate experienced by the sidewall of the target are reduced, reflecting the diminished penetration capability of the TEFP as the wall thickness increases. In addition to the reduction in strain and strain rate, the adiabatic temperature rise also plays a critical role in the recrystallization process. As the liner thickness and stand-off distance increase, the impact velocity of the TEFP decreases, leading to a lower adiabatic temperature rise at the target sidewall. Insufficient temperature elevation can suppress the thermally activated processes of dislocation climb and grain boundary migration that are essential for dynamic recrystallization (Sakai et al., 2014; Huang and Logé, 2016). Consequently, the combined reduction in strain, strain rate, and adiabatic heating jointly contributes to the narrowing of the dynamic recrystallization zone. A further comparison of different stand-off distances reveals that, with increasing stand-off distance, the width of the dynamic recrystallization zone corresponding to both wall thicknesses decreases. This finding suggests that a higher stand-off distance similarly reduces the strain and strain rate at the target sidewall, thereby weakening the penetration capability. It is particularly significant that, under the condition of stand-off distance h=200 mm and wall thickness a=4.5 mm, the dynamic recrystallization zone exhibits the minimum width (only 53.4 μm), and the grain elongation and density in the SPD zone are lower than those under other conditions. This observation is fully consistent with the macroscopic result that the TEFP fails to perforate the target plate in this case.

Adjacent to the SPD zone is the plastic deformation region (Figure 8), where the grains exhibit varying degrees of torsional distortion while the grain boundaries remain clearly distinguishable. The analysis indicates that, with increasing stand-off distance and wall thickness, the extent of grain distortion in this region gradually decreases, further confirming the tendency of the TEFP penetration and damage capability to diminish as these two parameters increase.

In summary, during the transition from the free surface of the target sidewall to the interior matrix, the grain morphology exhibits a systematic evolutionary sequence: dynamically recrystallized grains, severely elongated grains within the SPD zone, and torsionally distorted grains. The characteristics and deformation intensity of these distinct plastic deformation regions effectively characterize the penetration capability of the TEFP under varying stand-off distances and wall thicknesses, thereby elucidating the underlying damage mechanism at the microscopic scale.

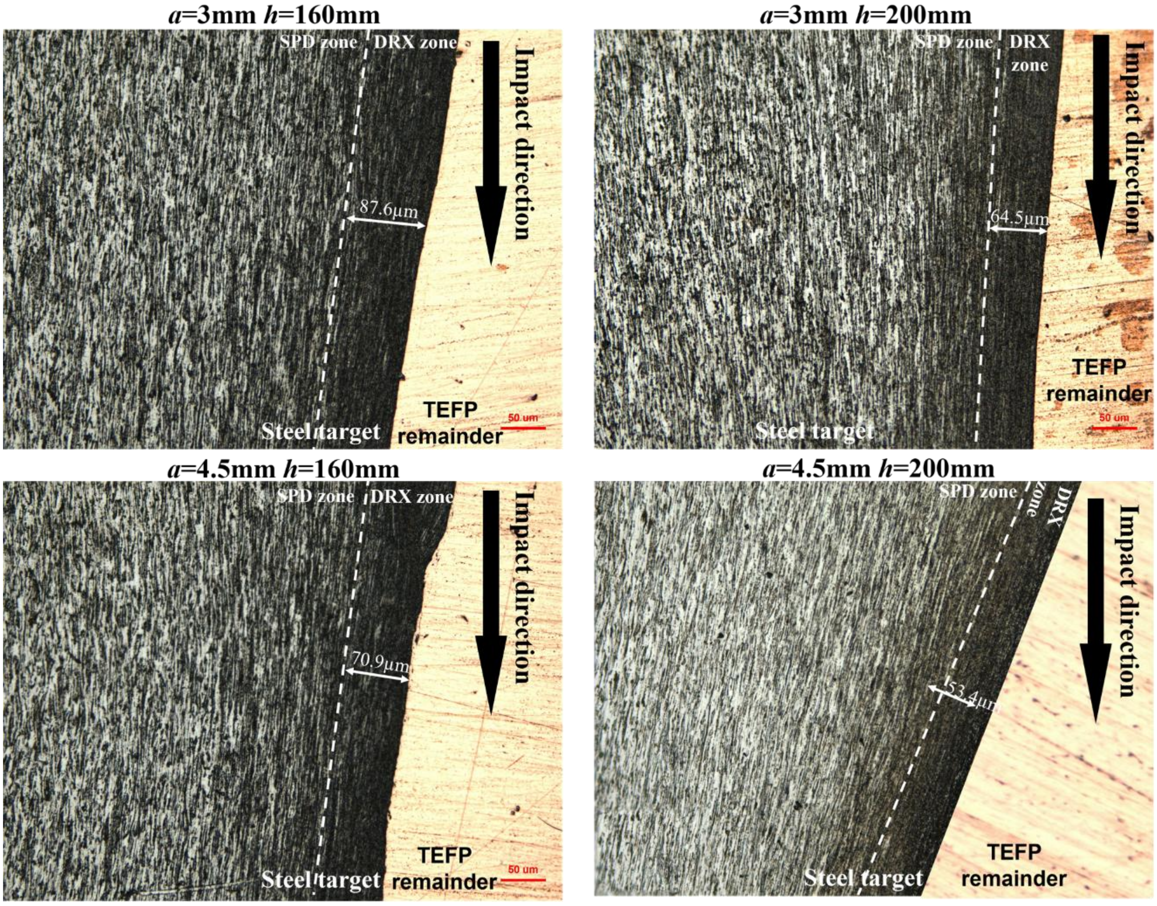

Figure7 *Microstructural features of metal grains on the sidewall of the steel target after high-velocity impact by the uniform-thickness liner TEFP*

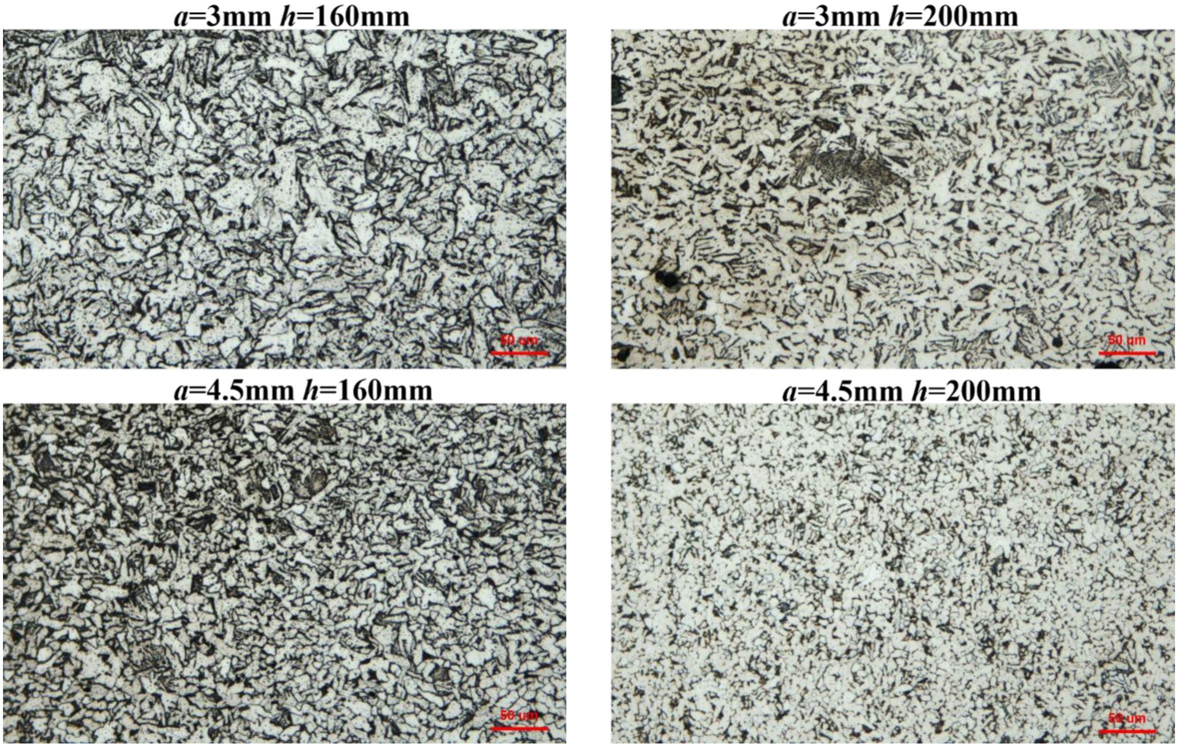

Figure8 *Microstructural features of metal grains in the plastic deformation zone of the steel target after high-velocity impact by the uniform-thickness liner TEFP*

4 NUMERICAL SIMULATION OF PENETRATION

4.1 Numerical Simulation Model

To investigate the formation and penetration characteristics of the TEFP, a three-dimensional numerical model was established using the ANSYS/LS-DYNA software, as shown in Figure 9. Based on structural symmetry, a one-quarter model was constructed to simplify the computation, and the corresponding symmetry constraints were applied. The supporting effect of the target holder was simplified as a full constraint on the boundary of the target plate.

Considering that the destruction effect of far-field detonation on steel structures is negligible, all models were discretized using the Lagrangian algorithm with eight-node hexahedral elements (SOLID164). The liner was meshed with a butterfly-shaped grid to ensure computational symmetry and stability. The contact settings were configured as follows: sliding penalty contact (CONTACT_SLIDING_ONLY_PENALTY) was applied between the explosive and the liner; automatic single-surface contact (CONTACT_AUTOMATIC_SINGLE_SURFACE) was assigned to the liner itself to suppress mesh penetration and distortion during the forming process; and the erosive penetration between the projectile and the target was simulated using eroding surface-to-surface contact (*CONTACT_ERODING_SURFACE_TO_SURFACE). According to previous studies (Gao et al., 2024), the influence of detonation products on the liner becomes negligible approximately 24 μs after initiation. Therefore, in the numerical model, the explosive elements were deleted at that moment using the *MAT_ADD_EROSION keyword.

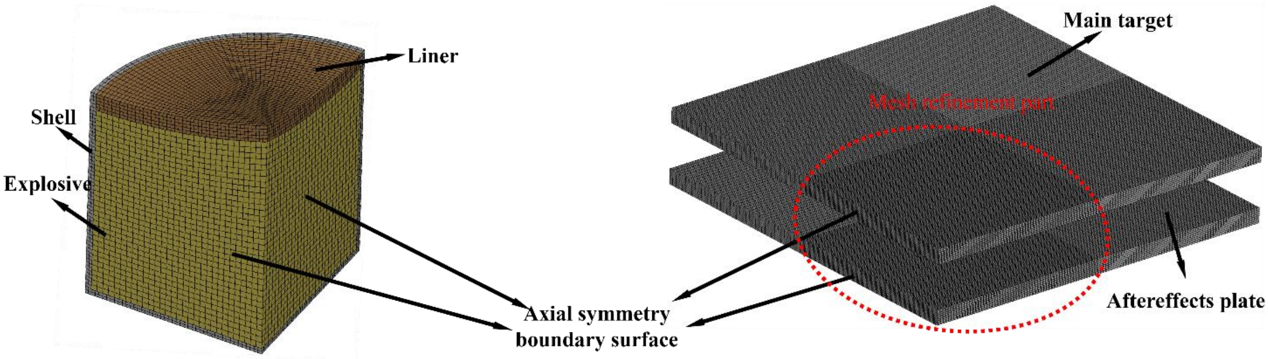

(a) TEFP warhead

(b) Q235 target plate

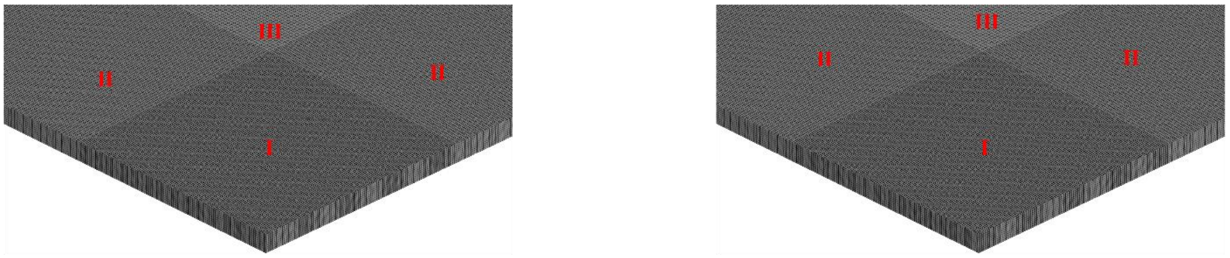

(c) Subdivided grid regions of the main target

(d) Subdivided grid regions of the aftereffects target

Figure9 *Finite element model: (a) TEFP warhead; (b) Steel target; (c) Mesh of the main target; (d) Mesh of the witness target*

The computational model was meshed using the HyperMesh software. To enhance computational efficiency while ensuring accuracy in critical regions, local mesh refinement was applied to the contact area between the TEFP and the target plate (Figure 9). The specific configurations were as follows: Region I (core contact zone) employed an element size of 1mm×1 mm×1 mm; Region II (adjacent influence zone) used 2mm×1mm×1mm; and Region III (remaining area) adopted 2mm×2 mm×1mm . In the numerical simulation, the explosive, plastic casing, liner, and target plate were all treated as homogeneous and continuous media. The entire explosion and penetration process was assumed to be adiabatic, and gravitational effects were neglected.

4.2 Constitutive Models and Material Parameters

4.2.1 Explosive Material Model

The explosive charge of the TEFP warhead, composed of a composite explosive with RDX as the base component composition , as referenced in Tang et al. (2025), was modeled using the *MAT_HIGH_EXPLOSIVE_BURN constitutive model in combination with the Jones–Wilkins–Lee (JWL) equation of state. The expression of the JWL equation of state is presented in Equation (1).:

$$P = A\left(1 - \frac{\omega}{R_1 V}\right)e^{-R_1 V} + B\left(1 - \frac{\omega}{R_2 V}\right)e^{-R_2 V} + \frac{\omega E}{V} \tag{1}$$

In this equation of state, P represents the instantaneous pressure generated by the detonation of the explosive, commonly referred to as the detonation pressure. The state parameters *A*, R1, *B*, R2, and ω are empirical constants obtained through extensive calibration based on numerous explosive initiation experiments. V denotes the specific volume, and E is the internal energy per unit volume of the explosive. The relevant parameters of the explosive are listed in Table 1.

Table 1 Explosive parameters (Tang et al., 2025)

ρ/(g·cm^{-3})	**D/(cm·μs^{-1})**	**A/GPa**	**B/(GPa)**	**R_1**	**R_2**	**P_{CJ}/GPa**

1.304	0.6505	337.17	9.0368	4.9	1.3	13.793

4.2.2 Material Models for Liner, Casing, and Target Plate

To accurately describe the dynamic response of the metallic liner under explosive loading, the circumferential impact and compression of the plastic casing by the detonation wave, as well as the high-temperature, high-pressure, and high–strain-rate failure modes occurring during the high-velocity impact of the TEFP on the target plate, this study employed the Johnson–Cook (J–C) constitutive model together with the Grüneisen equation of state to simulate the formation and penetration process of the TEFP. In the J–C model, the yield stress of the material is expressed as:

$$\sigma_y = \left[A_1 + B_1 \left(\bar{\varepsilon}^P \right)^n \right] \left(1 + C \ln \dot{\varepsilon}^* \right) \left[1 - \left(T^* \right)^m \right]$$

(2)**Erro! Fonte de referência não encontrada.**

In this equation, A_1denotes the yield stress constant of the material under small strain conditions; B_1represents the strain hardening coefficient; nis the strain hardening exponent; Cis the strain rate sensitivity coefficient; and mis the thermal softening coefficient — all of which are determined experimentally. This model characterizes the material's strain hardening, strain rate hardening, and thermal softening behaviors through three multiplicative terms. ε^pis the equivalent plastic strain of the material, and σ_yis the yield stress corresponding to the dimensionless effective plastic strain, referenced to the initial strain rate ε ̇^*. Trepresents the current temperature of the material, T_"room" is the room temperature, and T_"melt" is the melting temperature of the material. The term T^*=(T-T_"room")/(T_"melt" -T_"room")defines the normalized (relative) temperature. The material parameters and equations of state used in the numerical calculations are summarized in Tables 2 and 3.

Table 2 Parameters of the Johnson-Cook material model (Gao et al., 2024; Johnson and Cook, 1985; Zhang et al., 2023)

Material	**Material mechanical properties**					
Oxygen-Free High-Conductivity copper	**ρ/(g·cm^{-3})**	**G/(GPa)**	**A_1/(GPa)**	**B_1/(GPa)**	**C**	**n**	**m**
	8.96	46	0.9E-3	2.92E-3	0.025	0.31	1.09
	T_m/(K)	**T_r/(K)**	**D_1**	**D_2**	**D_3**	**D_4**	**D_5**
	1356	294	0.54	4.89	-3.03	0.014	1.12
Q235 steel	**ρ/(g·cm^{-3})**	**G/(GPa)**	**A_1/(GPa)**	**B_1/(GPa)**	**C**	**n**	**m**
	7.8	75	0.2938	0.2302	0.065	0.578	0.706
	T_m/(K)	**T_r/(K)**	**D_1**	**D_2**	**D_3**	**D_4**	**D_5**
	1795	300	0.472	18.728	-7.805	-0.019	3.811
Resin plastic	**ρ/(g·cm^{-3})**	**G/(GPa)**	**σ_y(MPa)**	**C_1**	**S_1**	**S_2**	**S_3**
	1.196	2.4	0.05	0.1933	3.49	-8.2	9.6

Table3 Parameters of the Grüneisen equation of state (Gao et al., 2024; Johnson and Cook, 1985; Zhang et al., 2023)

Material	**C_1**	**S_1**	**S_2**	**S_3**	**γ_0**	**α**
Oxygen-Free High-Conductivity copper	0.394	1.489	0	0	2.020	0.470
Q235 steel	0.457	1.490	0.6	0	2.170	0

4.3 Experimental and Numerical Results Comparison

The comparative results of the experimental and numerical simulations for the perforation shapes on the front and back surfaces of the main target, as well as on the front surface of the witness target, are shown in Figure 10. It can be observed that the penetration hole dimensions produced by the uniform-thickness liner TEFP in the numerical simulations are consistent with those obtained in the experiments. A comparison between the experimental and simulated results shows that the maximum errors of the penetration hole diameters on the front surface (d_1) and back surface (d_2) of the main target are 4.2% and 11.1%, respectively. For the front surface penetration diameter (d_3) of the witness target, the maximum error is less than 10% under all conditions except for the case of a=4.5mm and h=200mm, where the deviation reaches 20%. This larger discrepancy is attributed to the fact that under this condition (a=4.5 mm, h=200 mm), the TEFP undergoes severe fragmentation before impacting the witness target (Target B). The stochastic nature of fragment dispersion and impact locations introduces greater uncertainty in the measured penetration diameter on Target B, which is inherently difficult to reproduce precisely in a deterministic numerical simulation. Therefore, the numerical simulation model established in this study can effectively reproduce both the liner formation and the penetration processes of the shaped-charge warhead analyzed in this chapter.

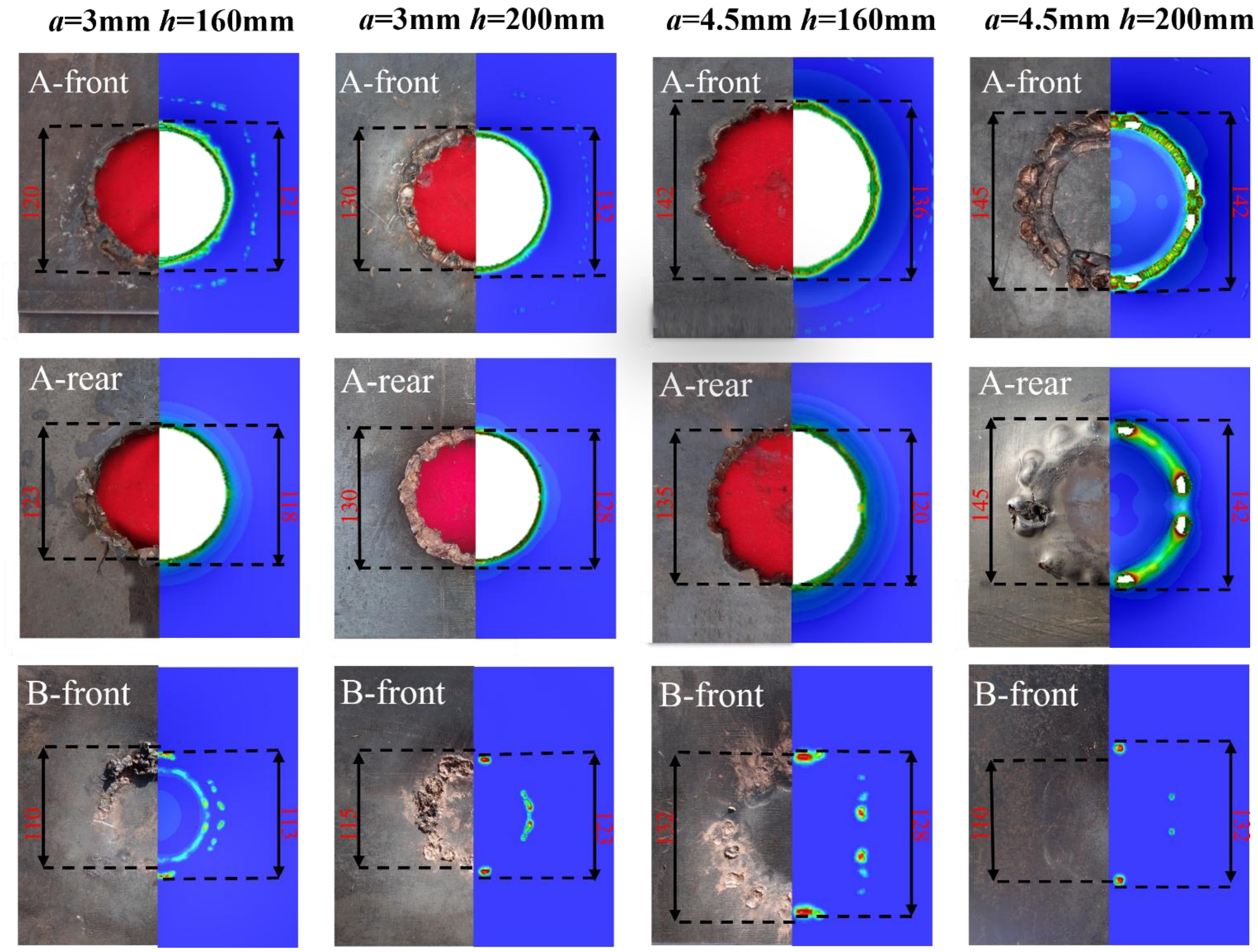

Figure10 *Comparison of penetration hole morphology between experimental results and numerical simulations (Unit: mm)*

5 FORMATION AND PENETRATION OF TEFP WITH UNIFORM-THICKNESS LINER

5.1 Formation Process Analysis of TEFP with Uniform-Thickness Liner

To further investigate the effects of stand-off distance and wall thickness on the formation and penetration performance of the TEFP, as well as to reveal its penetration and damage mechanisms against metal targets, additional numerical simulation cases were conducted using uniform-thickness liners of 1.5 mm and 6 mm.

Figure 11 illustrates the dynamic evolution of the pressure on the inner wall of the liner after the detonation of TEFP warheads with four different uniform-thickness. By analyzing the coupling relationship between the pressure curves and the detonation wave propagation, the critical influence of wall thickness on energy transfer during TEFP formation can be revealed.

In the initial stage (t=8 μs), the annular detonation wave first acts on the middle-to-apex region of the liner, forming an initial high-pressure zone. The corresponding inner wall pressure curve exhibits a rapid rise followed by a decline, with the peak point representing the initial center of action of the detonation wave. A clear trend is observed: the greater the wall thickness, the higher the inner wall pressure at this instant. This is attributed to the fact that increased wall thickness leads to greater mass and enhanced inertia of the liner, making it more difficult for the detonation wave to drive its collapse and deformation. Consequently, more energy accumulates on the inner surface, thereby elevating the pressure.

Later (t=8.5 μs), as the detonation wave reaches the apex of the liner, a fan-shaped high-pressure zone is generated, causing the pressure curve to display a complex "brief rise-fall-rise-fall" oscillation. After an initial spike, the pressure decays near the central axis. This attenuation is mainly driven by the radial convergence of rarefaction waves governed by geometrical symmetry, whose superposition heavily intensifies the unloading process. Elsewhere within the fan-shaped zone, the pressure drops first and then recovers; the lowest pressure occurs at the initial interaction center, where the unloading from rarefaction waves acts earliest. At this specific time, the inner surface pressure still shows a marked increase with greater wall thickness. Beyond the mass effect discussed earlier, a thicker liner physically retards the penetration of the rarefaction waves, thereby delaying the unloading process and prolonging the high-pressure duration.

As the detonation wave continues to propagate (t=9 μs), new high-pressure zones emerge at the apex and the middle-to-rear sections of the liner, whereas the pressure in the initial interaction region has decreased substantially. At this stage, the pressure curve exhibits a characteristic "gradual decline-rise-decline" pattern, with its peak corresponding to the subsequent interaction region of the detonation wave. Outside this specific area, pressures at all other locations are significantly lower than those at the previous instant. This overall drop is primarily attributed to the continuous unloading effect of the rarefaction waves and the intrinsic attenuation of the detonation wave itself.

Finally (t=9.5 μs), the detonation wave reaches the tail of the liner, forming a localized high-pressure zone. Under the combined action of the detonation products, the inversion formation of the TEFP is successfully completed.

In summary, the increase in liner wall thickness influences energy transfer in two ways: first, the increased mass elevates the difficulty for the detonation wave to drive the liner; second, it retards the unloading of rarefaction waves, maintaining the inner wall pressure at a higher level. The rise in inner wall pressure indicates that a larger portion of the detonation energy is partitioned into the liner's internal energy rather than its kinetic energy. Consequently, the final kinetic energy obtained by the TEFP gradually decreases as the wall thickness increases. This mechanism clearly elucidates the critical constraining effect of wall thickness on TEFP formation efficiency and its subsequent penetration capability.

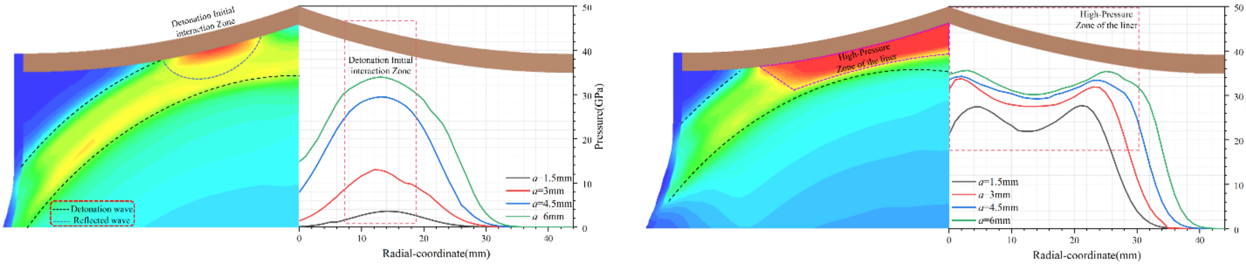

(a)The detonation wave propagation and the inner wall pressure of the line at 8μs

(b)The detonation wave propagation and the inner wall pressure of the line at 8.5μs

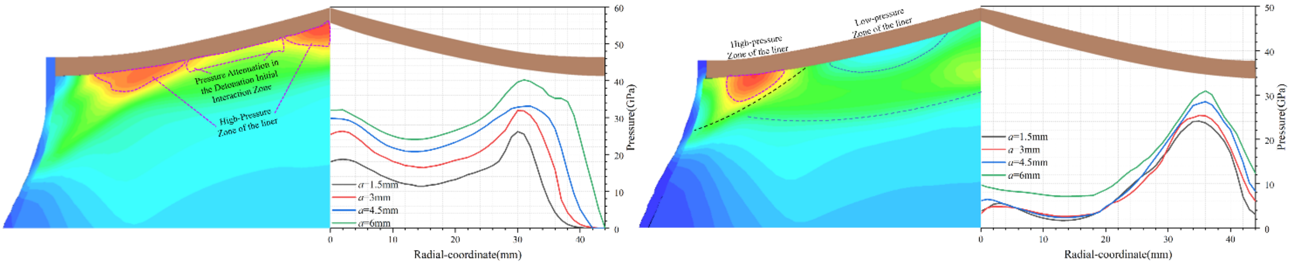

(c)The detonation wave propagation and the inner wall pressure of the line at 9μs

(d)The detonation wave propagation and the inner wall pressure of the line at 9.5μs

Figure11 *Pressure variation curves on the inner wall of the liner subjected to the detonation wave at different times*

The morphological comparison (Figure 12(a)) shows that as the liner wall thickness decreases, the length and head diameter of the TEFP gradually increase, while the tail diameter correspondingly decreases. It is noteworthy that for the structure with the largest wall thickness (a=6mm), the head remained unopen even after the detonation process was completed.

The energy analysis (Figure 12(b)) indicates that as the liner wall thickness decreases, both the total energy and kinetic energy of the TEFP gradually increase, while the internal energy correspondingly decreases. This occurs because a thinner liner is more easily driven by the detonation, which enhances the efficiency of energy transfer from the explosive to the liner, resulting in a greater proportion of the explosive energy being converted into kinetic energy. This energy partitioning provides a material-independent design principle for tailoring charge configurations to specific target materials. For high-strength targets, thinner liners that maximize kinetic energy conversion are preferred to enhance penetration depth. For brittle targets such as concrete or rock, thicker liners that retain higher internal energy can promote early-stage fragmentation, thereby expanding the fragment damage zone—an effect consistent with the observation that the fragment damage zone area on Target A substantially exceeded the perforation diameter. For ductile, moderate-strength targets such as Q235 and aluminum alloys, an intermediate wall thickness offers a practical balance between kinetic energy delivery and structural integrity.

The velocity distributions (Figures 12(c) and 12(d)) show that as the liner wall thickness decreases, the total velocity, axial velocity (V_x), and radial velocity (V_y) of the TEFP all exhibit a decreasing trend. Along the direction from the head to the tail, both total and axial velocities gradually decrease and then drop sharply near the tail. In contrast, the radial velocity first decreases slowly and then rises sharply at the tail. The sudden increase in radial velocity at the tail originates from the fact that the detonation wave at that region acts more radially, causing a greater portion of the energy to be converted into radial expansion. This pronounced difference between axial and radial velocities leads to continuous radial expansion and axial stretching of the TEFP during the formation process. Moreover, the velocity mismatch between the tail and other regions induces extremely high stress during subsequent flight, eventually resulting in detachment of the tail from the main body.

Figure 13 illustrates the formation and evolution process of TEFPs with four different liner wall thicknesses. Under the combined action of the detonation wave and detonation products, the head of the TEFP first undergoes plastic deformation and forms an opening, while the continuous radial velocity component causes ongoing radial expansion. Because the tail region exhibits a greater radial velocity but a lower axial velocity at t=25 μs , its velocity becomes mismatched with that of the main body, resulting in significant stress. When this stress exceeds the material strength limit, the tail ruptures and detaches, generating fragments that subsequently penetrate the target plate (corresponding to the macroscopic fragment-damage zone). After the tail separation, the remaining TEFP continues to expand and move forward, with large strains developing in the head and residual tail regions. Once the expansion reaches a certain extent and the internal stress again surpasses the material limit, the TEFP fractures along the axial direction, ultimately producing an annular distribution of fragments.

Based on the above analysis, the formation process of the uniform-thickness liner TEFP can be divided into three stages. In the stable expansion stage, the head of the TEFP forms an opening while the overall structure remains intact and expands steadily; at this time, the expansion diameter of the head is smaller than that of the tail. In the tail separation stage, a velocity mismatch between the tail and the main body generates extremely high stress, causing the tail to gradually rupture and detach. In the fracture and fragmentation stage, after the tail separates, the remaining TEFP experiences high stress due to velocity differences and continuous radial expansion, leading to progressive axial fracture and the formation of an annular fragment cluster. During this final stage, the head diameter gradually becomes larger than that of the tail.

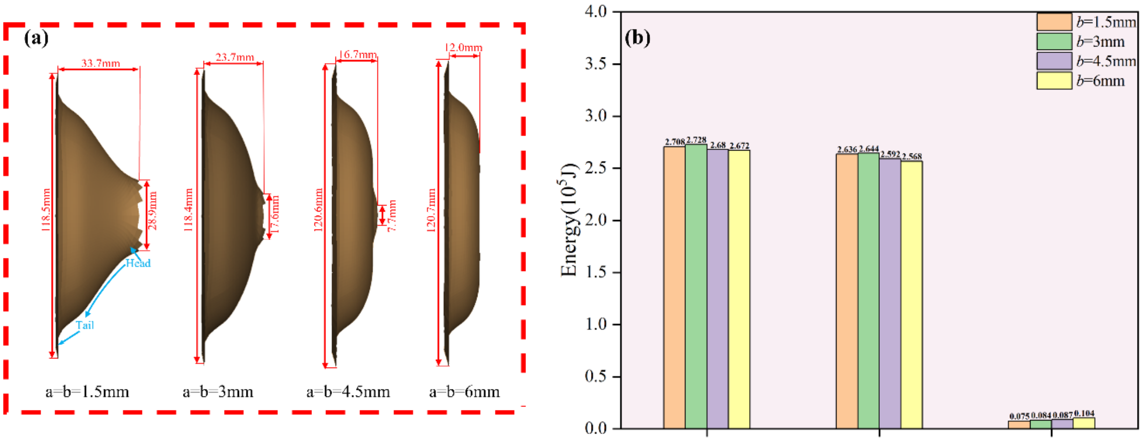

(a) Comparison of TEFP morphologies for different structures at t = 25 μs

(b) Comparison of TEFP energy for different structures at t = 25 μs

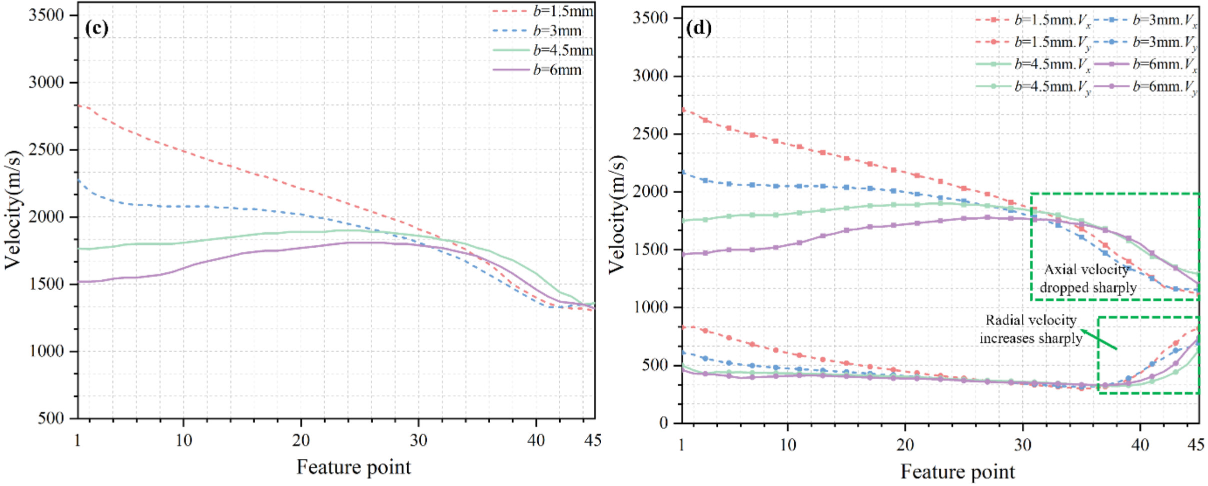

(c) Comparison of TEFP velocities for different structures at t = 25 μs

(d) Comparison of axial and radial velocities of TEFP for different structures at t = 25 μs

***Figure12** Velocity, energy, and morphology of TEFPs from different uniform-thickness liner structures at t=25μs*

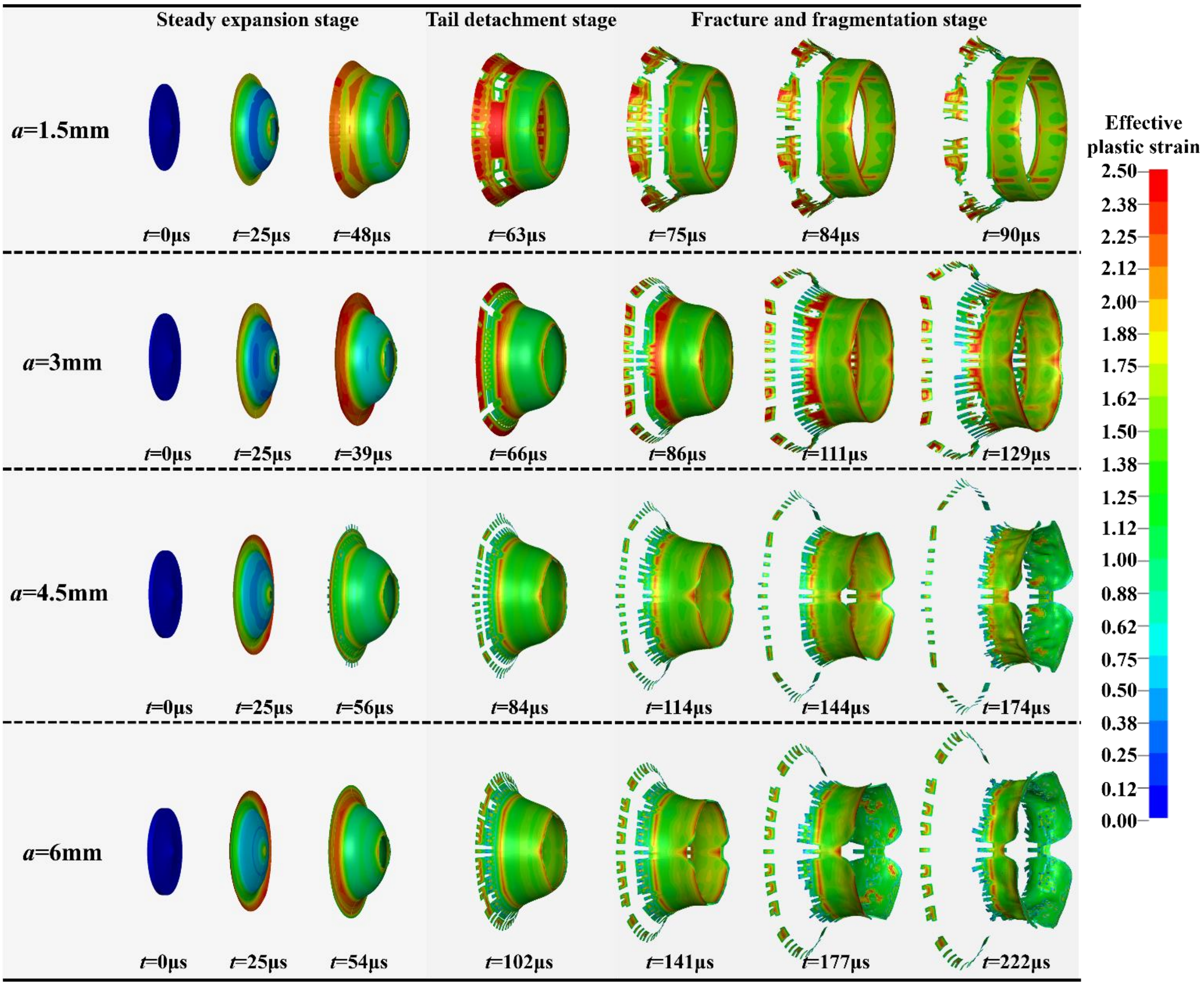

Figure13 *Formation and evolution processes of TEFPs from different uniform-thickness liner structures*

5.2 Typical penetration process of uniform-thickness liner TEFP

Figure 14 presents the penetration process of the target plates by two uniform-thickness liner TEFPs under experimental conditions. The numerical simulation results are consistent with the experimental observations: the TEFP with a wall thickness of a=3mm is able to penetrate the main target at both stand-off distances of h=160 mm and h=200 mm, whereas the TEFP with a wall thickness of a=4.5mm can penetrate the main target only at h=160 mm and fails to achieve full perforation at h=200 mm. The analysis indicates that, under all conditions, the TEFP has already entered the fracture and fragmentation stage when impacting the main target. At the same stand-off distance, the 3 mm thick liner exhibits a more favorable formation morphology compared with the 4.5 mm thick liner. Specifically, at h=160mm, the 3 mm TEFP produces residual fragments and shear blocks with relatively high velocities after penetrating the target plate. In other conditions, although certain residual fragments with moderate velocity are also generated, the shear blocks move at lower velocities and lack further penetration capability. From the perspective of the damage process to the witness target, at h=160 mm , the 3 mm TEFP causes damage through the combined action of the residual fragments and shear blocks that pass through the main target. At h=200mm , the damage is mainly attributed to the residual fragments. For the TEFP with a 4.5 mm wall thickness, the secondary damage—whether at h=160 mm or h=200 mm —is primarily caused by residual fragments that penetrate the main target, and the extent of damage decreases with increasing stand-off distance.

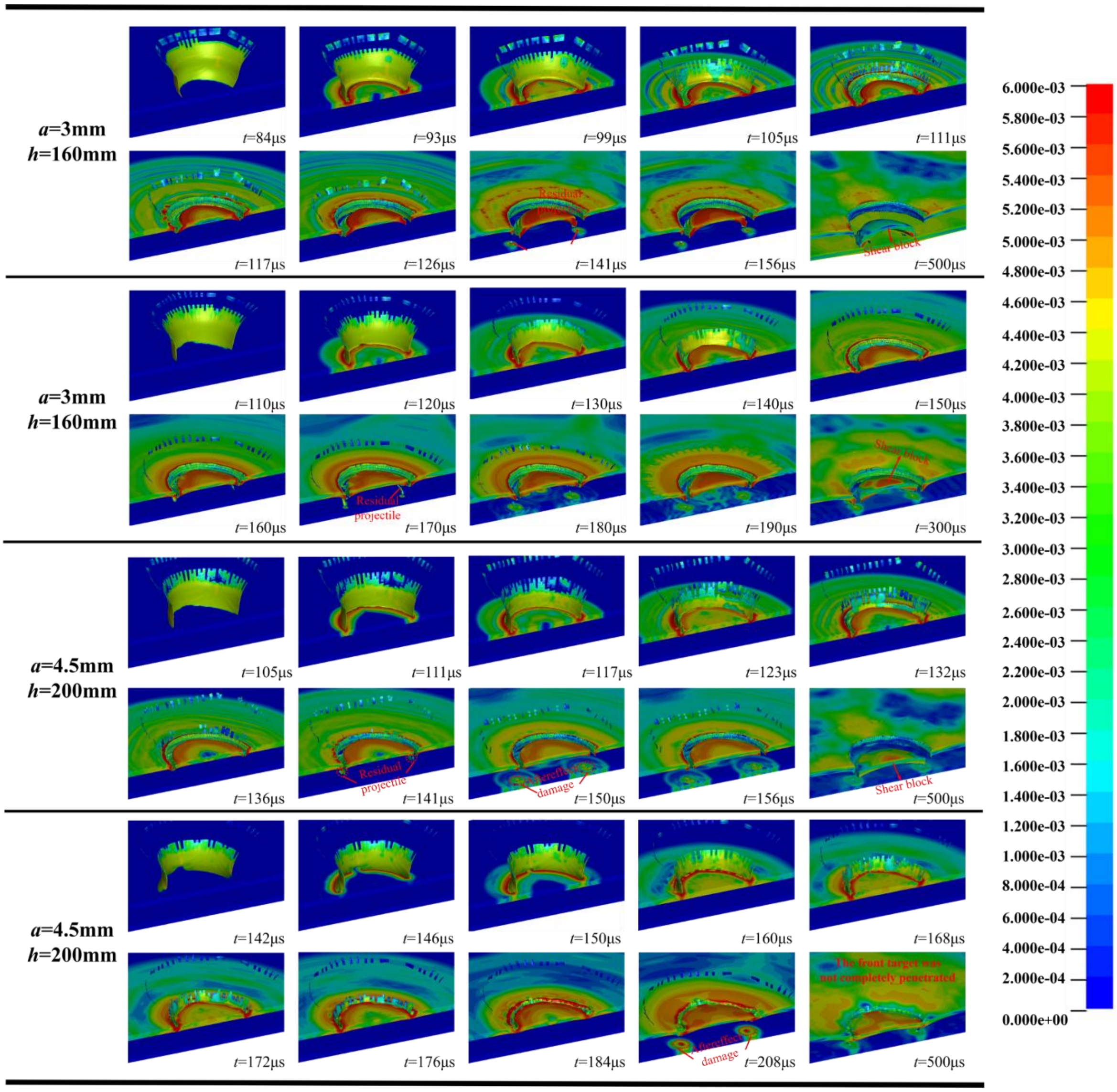

***Figure14** Penetration processes of TEFPs from two uniform-thickness liner structures into the metal target under experimental conditions*

Figures 15 and 16 provide a more intuitive depiction of the detailed penetration processes of the two TEFPs into the main target. At a stand-off distance of h=160mm , the TEFP with a wall thickness of a=3mm penetrates obliquely at a relatively small incident angle (θ=65°). After the initial crater formation, its radial velocity component drives continuous expansion of the penetration hole. The head gradually bends, flattens, and eventually erodes, while the remaining portion continues its oblique penetration and ultimately perforates the target. At the same stand-off distance, the TEFP with a=4.5mm penetrates nearly vertically (θ=87°); its head shows no significant bending and mainly expands the hole through outward radial extrusion, causing a gradual increase in the aperture. During this process, the non uniform reactive force of the target plate progressively deflects the penetration path from vertical to oblique until complete perforation occurs. When the stand-off distance increases to h=200 mm, the incident angles of both TEFPs further increase. The 3 mm TEFP penetrates at an incident angle of approximately 91°, with a process similar to that of the 4.5 mm TEFP at h=160mm —accompanied by hole expansion and gradual inclination, though with a smaller degree of deflection. In contrast, the 4.5 mm TEFP exhibits a markedly oblique penetration at a large incident angle of 103°. Its penetration process differs significantly: during the early and middle stages, the TEFP first compresses the target plate radially inward, and subsequently transitions to outward expansion under the combined effects of its own radial expansion velocity and the reactive force of the target plate. In theory, if sufficient kinetic energy were retained, full perforation could still occur even under a large oblique incident angle. However, under this condition, the TEFP had already undergone extensive fragmentation prior to impact, resulting in low kinetic energy and poor structural integrity, and therefore failed to completely perforate the target plate. Comprehensive analysis of these typical penetration processes reveals that the incident angle θ of a TEFP upon striking the target varies with both stand-off distance and liner wall thickness, and has a significant influence on its penetration behavior. To systematically elucidate the underlying mechanisms, the penetration process in this study is classified into three typical modes (Figure 17: positive cutting (Mode I, $0^{\circ}<\theta\leq 85^{\circ}$), accurate cutting (Mode II, $85^{\circ}<\theta\leq 95^{\circ}$), and reverse cutting (Mode III, $95^{\circ}<\theta<180^{\circ}$). This classification is derived from the systematic numerical analysis of the penetration behavior observed in the present study under the specific conditions of uniform-thickness liners (a = 1.5–6 mm) and stand-off distances (h = 100–300 mm). It should therefore be regarded as an empirical categorization based on the limited parametric range investigated, rather than a universal theoretical law. Its applicability is confined to the liner thickness and stand-off distance ranges considered herein.

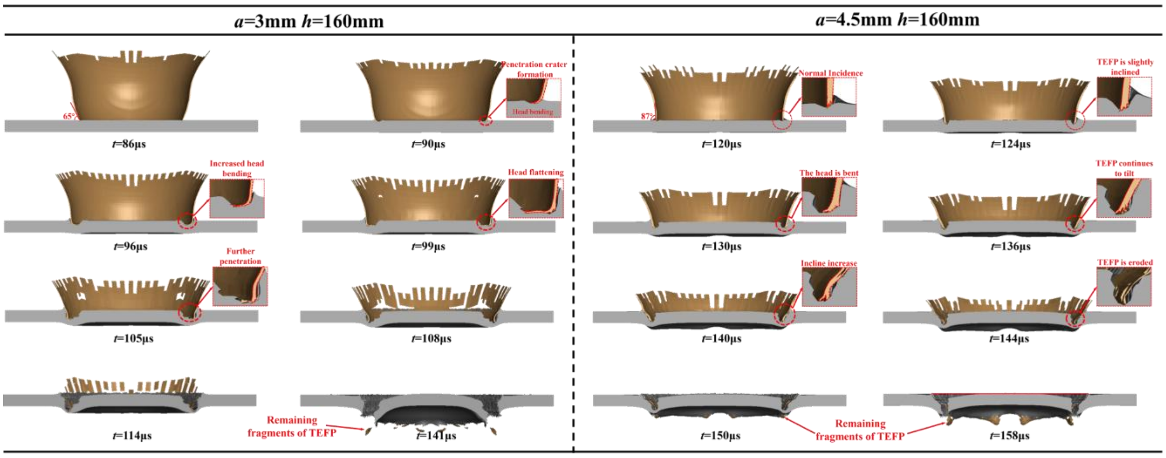

Figure 15 Penetration processes of TEFPs from two uniform-thickness liner structures into the main target at h=160 mm

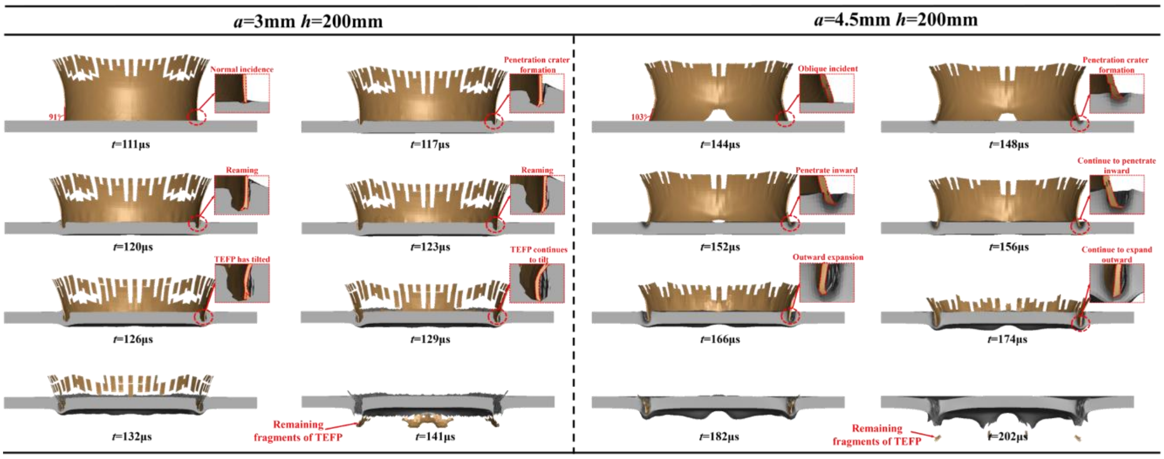

Figure 16 Penetration processes of TEFPs from two uniform-thickness liner structures into the main target at h=200mm

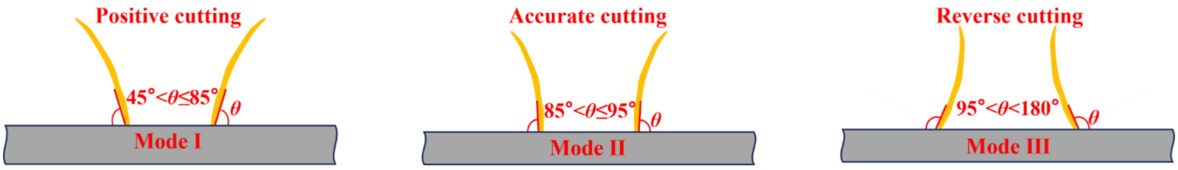

Figure17 Three typical penetration modes of TEFPs from uniform-thickness liners

Numerical simulations were conducted to extract and fit the incident angle ϑ of TEFPs at different stand-off distances, yielding the variation curves of θ with stand-off distance h (Figure 18) and the corresponding engineering formulas (Equations (1)–(3)). The curves show that the incident angle θ increases continuously with increasing stand-off distance h. Moreover, at the same stand-off distance, TEFPs with larger liner wall thickness exhibit greater incident angles, as their longer flight times result in more pronounced angular deviation. This indicates that increasing the wall thickness enables the TEFP to reach the accurate cutting mode within a shorter flight distance, thereby affecting the range of stand-off distances at which effective target penetration can occur. In addition, a larger wall thickness also leads to reduced kinetic energy of the TEFP, further diminishing its penetration capability.

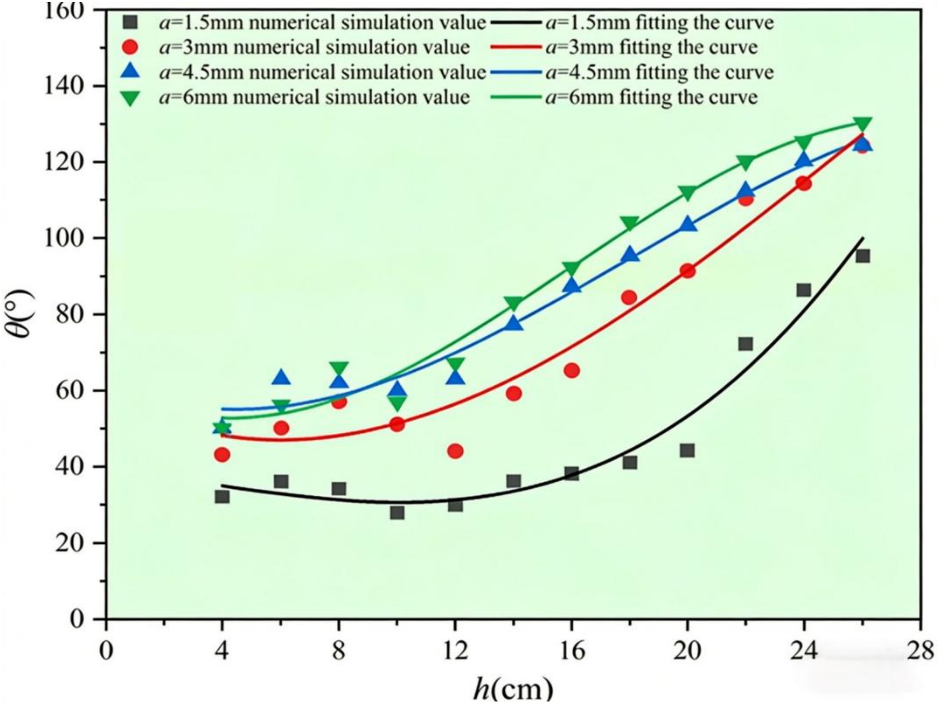

Figure18 *Variation curves of TEFP incident angle versus stand-off distance for different liner thicknesses*

$$f(x) = B + \sum_{i=1}^{3} B_i x^i \quad (1)$$

$$B = 62.095;\ B_1 = -3.364;\ B_2 = 0.429;\ B_3 = -0.008 \quad (2)$$

$$B = 61.768;\ B_1 = -4.628;\ B_2 = 0.629;\ B_3 = -0.014 \quad (3)$$

In these expressions, f(x) denotes the incident angle, while Equations (2) and (3) specify the corresponding parameters for calculating the incident angles of uniform-thickness liner TEFPs with wall thicknesses of 3 mm and 4.5 mm, respectively.

6 CONCLUSIONS

This study focuses on the uniform-thickness liner TEFP warhead. Through penetration experiments conducted under varying stand-off distance and liner wall thicknesses, combined with microscopic characterization and dynamic simulations, the effects and underlying mechanisms of liner structure and stand-off distance on penetration and damage performance were revealed across macro and micro scales. Furthermore, the matching relationships among wall thickness, stand-off distance, and final damage effectiveness were clarified. The main conclusions are as follows:

(1) For the 88-mm charge diameter considered in this work, the kinetic energy, axial velocity, and radial velocity of the TEFP all decrease with increasing liner wall thickness. Its formation process can be divided into three stages: stable expansion, tail separation, and fracture and fragmentation. During this process, both the diameter and length of the TEFP continuously increase; however, the velocity mismatch between the tail and the main body causes tail separation in the second stage, while the remaining portion undergoes further fracture in the third stage.

(2) Microscopic analysis indicates that although the macroscopic damage of the target plate caused by the TEFP is predominantly governed by shear failure, its penetration capability decreases with increasing stand-off distance and liner wall thickness. Consequently, the damage mode at the bottom of the penetration crater gradually changes from localized

shear to localized tensile failure. During the transition from the sidewall of the penetration hole toward its interior, the target material exhibits three typical grain morphologies: dynamic recrystallization, severe elongated deformation, and twisted deformation. Moreover, the width of the dynamic recrystallization zone decreases as both wall thickness and stand-off distance increase.

(3) Increases in liner wall thickness (a) and stand-off distance (h) lead to a gradual reduction in the penetration capability of the TEFP, and in extreme cases, complete loss of perforation ability, while the penetration crater diameter increases correspondingly (up to 1.6× CD). The incident angle (θ) at impact rises with both parameters, and the penetration process is classified into three characteristic modes: positive cutting (Mode I, $0° < \theta \leq 85°$), accurate cutting (Mode II, $85° < \theta \leq 95°$), and reverse cutting (Mode III, $95° < \theta < 180°$). The entire penetration event comprises three stages: crater initiation, bulge development, and shear block formation.

Future research directions include: (i) extending the parametric investigation to variable-thickness liner configurations, which may offer additional degrees of freedom for optimizing the trade-off between penetration depth and hole-expansion diameter; (ii) exploring the influence of liner material composition (e.g., reactive or composite liners) on TEFP damage mechanisms; and (iii) developing analytical models to predict TEFP penetration performance across a broader range of charge calibers and target materials, thereby establishing a more generalized design framework for engineering applications.

Author’s Contributions: Writing - original draft,Qingxin Qin; Test technical support, Chong Ji, Xin Wang; Writing - review & editing,Gang Wu, Xin Wang; Numerical simulation technical support, Weijian Tang, Yuxuan Gao.

Editor: Marcilio Alves

References

Cardoso, D., & Teixeira-Dias, F. (2016). Modelling the formation of explosively formed projectiles (EFP). International Journal of Impact Engineering, 93, 116–127.

Chen, C., Wang, X. M., & Li, W. B. (2015). Effect of matching of detonation waveform with liner configuration on the rod-like jet formation. Explosion and Shock Waves, 35(6), 812–819. (in Chinese)

Dehestani, P., Fathi, A., & Daniali, H. M. (2018). Numerical study of the stand-off distance and liner thickness effect on the penetration depth efficiency of shaped charge process. Proceedings of the Institution of Mechanical Engineers, Part C: Journal of Mechanical Engineering Science, 233(3), 977–986.

Fu, J., Chen, Z., & Hou, X. (2013). Simulation and experimental investigation of jetting penetrator charge at large stand-off distance. Defence Technology, 9(2), 91–97.

Gao, Y. X., Ji, C., & Wang, X. (2024). Oblique penetration performance of explosively formed projectile (EFP) on 6061 aluminum target: Experiments and simulations. Latin American Journal of Solids and Structures, 21(1), e515.

Guo, H., Zheng, Y., & Yu, Q. (2019). Penetration behavior of reactive liner shaped charge jet impacting thick steel plates. International Journal of Impact Engineering, 126, 76–84.

Han, W., He, Y., & Shen, X. J. (2019). Investigation of EFP forming and penetration of Ta/Zr double-layered shaped charge liner. Journal of Ordnance Equipment Engineering, 40(4), 163–167, 173. (in Chinese)

Hu, Y., Wang, Y., & Ji, C. (2026). Forming mechanism and penetration performance of toroidal explosively formed projectile shaped charge. Journal of the Brazilian Society of Mechanical Sciences and Engineering, 48, Article 127.

Huang, K., & Logé, R. E. (2016). A review of dynamic recrystallization phenomena in metallic materials. Materials & Design, 111, 548–574.

Johnson, G. R., & Cook, W. H. (1985). Fracture characteristics of three metals subjected to various strains, strain rates, temperatures and pressures. Engineering Fracture Mechanics, 21(1), 31–48.

Ji, Q., Wang, Z. J., & Yi, J. Y. (2021). Numerical study on the formation and penetration process of nylon jet from annular shaped charge. Journal of Ordnance Equipment Engineering, 42(5), 134–138, 190. (in Chinese)

Li, Z. T., Wang, S. Y., Sun, S. J., Jiang, J. W., & Men, J. B. (2025a). Influence and optimization of asymmetric annular shaped charge structure on penetration characteristics. Journal of Ordnance Equipment Engineering, 46(4), 115–123. (in Chinese)

Li, Z. T., Wang, S. Y., Sun, S. J., Jiang, J. W., & Men, J. B. (2025b). Analysis of influencing factors on the formation and penetration characteristics of asymmetric hollow annular shaped charges. Explosion and Shock Waves, 45(1), 43–52. (in Chinese)

Liu, J. F., Long, Y., & Ji, C. (2017). The influence of liner material on the dynamic response of the finite steel target subjected to high velocity impact by explosively formed projectile. International Journal of Impact Engineering, 109, 264–275.

Liu, Y., Yin, J. P., Wang, Z. J., Zhang, X. P., & Bi, G. J. (2020). Formation and penetration of double-layer explosive charge EFP. Materials, 13(20), 4519.

Mehmannavaz, H., Ramezani, M., & Liaghat, G. (2021). A practical review study on shaped charge in the last two decades (2000–2020). International Journal of Protective Structures, 12(3), 317–346.

Richard, F., LaMar, T., & William, N. (2010). Toroidal warhead development. In Proceedings of the 25th International Symposium on Ballistics (pp. 861–865). Beijing.

Sakai, T., Belyakov, A., Kaibyshev, R., Miura, H., & Jonas, J. J. (2014). Dynamic and post-dynamic recrystallization under hot, cold and severe plastic deformation conditions. Progress in Materials Science, 60, 130–207.

Shen, X. J., Zhao, Z. X., & Wang, X. (2025). Advances in novel structures and materials for shaped charge liners. Shock and Vibration, 2025, Article 9922621.

Tang, W. J., Ji, C., & Wang, Y. T. (2025). The influence of stand-off distance on the penetration characteristics of toroidal explosively formed projectile (TEFP). Latin American Journal of Solids and Structures, 22(2), Article e8415.

Wang, C., Xu, W., & Yuen, S. C. K. (2018). Penetration of shaped charge into layered and spaced concrete targets. International Journal of Impact Engineering, 112, 193–206.

Xu, W., Wang, C., & Yuan, J. (2019). Formation of a bore-center annular shaped charge and its penetration into steel targets. International Journal of Impact Engineering, 127, 122–134.

Yang, Z., Fu, J., & Liang, F. (2022). The influence of closed-cell W-shaped liner parameters on the penetration performance of integral annular shaped charge. Materials, 15, 7155.

Yin, J. P., Liu, Y. K., Wang, Z. J., Zhang, X. P., Zhi, J. Z., & Zhang, Y. (2023). Formation and penetration of PELE/EFP multi-mode warhead based on double-layer shaped charge. Journal of Energetic Materials, 41(1), 4–26.

Zhang, H., Zheng, Y. F., Yu, Q. B., Ge, C., Su, C. H., & Wang, H. F. (2022). Penetration and internal blast behavior of reactive liner enhanced shaped charge against concrete space. Defence Technology, 18(6), 952–962.